JACS
JOURNAL OF THE AMERICAN CHEMICAL SOCIETY
Article
pubs.acs.org/JACS

Colloidal Single-Layer Quantum Dots with Lateral Confinement Effects on 2D Exciton

Ho Jin,[†,⊥] Minji Ahn,[‡,§,∥,⊥] Sohee Jeong,[‡,§,∥] Jae Hyo Han,[‡,§,∥] Dongwon Yoo,[‡,§] Dong Hee Son,[*,†] and Jinwoo Cheon[*,‡,§,∥]

[†]Department of Chemistry, Texas A&M University, College Station, Texas 77843, United States
[‡]Center for Nanomedicine, Institute for Basic Science (IBS), Seoul 03722, Korea
[§]Yonsei-IBS Institute, Yonsei University, Seoul 03722, Korea
[∥]Department of Chemistry, Yonsei University, Seoul 03722, Korea

Supporting Information

ABSTRACT: Controlled lateral quantum confinement in single-layer transition-metal chalcogenides (TMCs) can potentially combine the unique properties of two-dimensional (2D) exciton with the size-tunability of exciton energy, creating the single-layer quantum dots (SQDs) of 2D TMC materials. However, exploring such opportunities has been challenging due to the limited ability to produce well-defined SQDs with sufficiently high quality and size control, in conjunction with the commonly observed inconsistency in the optical properties. Here, we report an effective method to synthesize high-quality and size-controlled SQDs of WSe_2 via multilayer quantum dots (MQDs) precursors, which enables grasping a clear picture of the role of lateral confinement on the optical properties of the 2D exciton. From the single-particle optical spectra and polarization anisotropy of WSe_2 SQDs of varying sizes in addition to their ensemble data, we reveal how the properties of 2D exciton in single-layer TMCs evolve with increasing lateral quantum confinement.

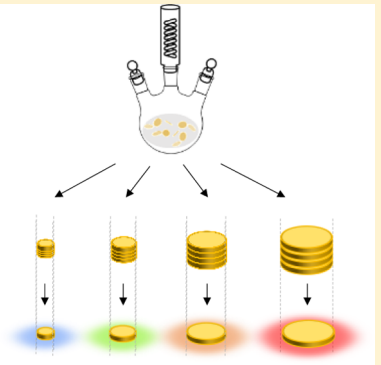

INTRODUCTION

In recent years, two-dimensional (2D) transition-metal chalcogenides (TMCs) have emerged as an important class of materials, where the new material properties are obtained by reducing the dimensionality.[1−6] For instance, the band gap of various semiconducting TMCs changes from an indirect to a direct gap with a concomitant appearance of strong exciton photoluminescence (PL) when they become single-layer thick.[7−12] The valley-selective excitation, providing a new degree of freedom to manipulate the material properties, also becomes possible in single-layer TMCs.[13−15] Furthermore, the reduced dimensionality and weaker screening effect can result in the formation of a strongly bound 2D exciton that largely determines the optical and charge transport properties of single-layer TMCs.[16−18] For single-layer TMCs, the reduction of the lateral size to the nanoscale can potentially combine the unique property of the 2D exciton with additional lateral confinement, creating the 'single-layer quantum dot (SQD)' that is distinctly different from more common quantum dots (QDs) derived from 3D crystals. To explore the properties of SQDs to reveal the effect of lateral confinement on 2D excitons in single-layer TMC materials, SQDs should not only satisfy the strict single-layer thickness requirement and lateral size controllability but also maintain single crystallinity without defects. However, there have been synthetic challenges to meet such criteria simultaneously. Some of the commonly employed methods utilize multistep exfoliation of the bulk TMCs to create SQDs.[19−22]

Since these methods typically require intense sonication and/or the use of highly reactive chemicals, such as Li^+, the resulting products tend to suffer from inhomogeneity of lateral size and/or thickness and difficulty maintaining single crystallinity without structural deformations. For example, the structural defects produce the trap states, such as vacancy or deformation of the crystal structure, which are known to form during the harsh exfoliation processes and can interfere with the characterization of the properties of the exciton, as in the case for common colloidal QDs. Therefore, despite the observation that the size-dependent PL suggests a possible lateral confinement effect,[19−24] understanding of the properties of 2D exciton in single-layer TMCs experiencing lateral quantum confinement has remained elusive.

In this study, we report a highly effective method to have high-quality, lateral size-controlled SQDs of TMCs with a circular shape using multilayer quantum dots (MQDs) as the precursor. The method involves the initial synthesis of disc-shaped MQDs with a controlled diameter followed by mild exfoliation via tandem molecular intercalation (TMI), producing SQDs that inherit the diameter and crystal phase of the initial MQDs without creating defects[25] (Scheme 1).

Received: July 6, 2016
Published: October 3, 2016

DOI: 10.1021/jacs.6b06972
J. Am. Chem. Soc. 2016, 138, 13253−13259

Scheme 1. New Chemical Synthetic Protocol That Provides High-Quality Colloidal Multilayer WSe_2 Quantum Dots (MQDs) with Controlled Lateral Size Using a Reaction Parameter Modulation (i.e., the Ratio of Surfactant to Metal Precursor)[a]

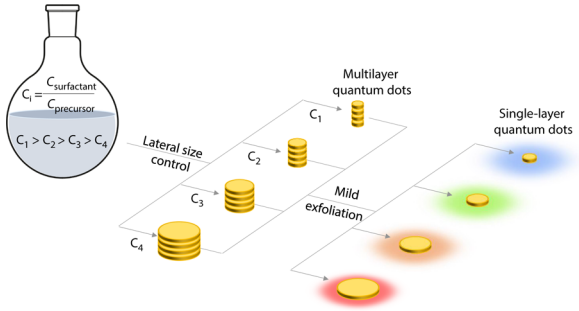

[a]Then, a mild TMI method produces single-crystalline SQDs with a lateral size identical to that of the MQDs prior to the exfoliation step.

Furthermore, from the single-particle optical spectra obtained from individual WSe_2 SQDs, clearly revealing the spectral details obscured in the ensemble optical spectra, the effects of the lateral quantum confinement on the optical transition in single-layer WSe_2 are unambiguously identified.

RESULTS AND DISCUSSION

WSe_2 is a representative 2D layered semiconducting material composed of repeating units of Se−W−Se triatomic layers, where W atoms are covalently bonded to Se atoms, while the layers are weakly bound by van der Waals force with 6.5 Å interlayer distances (Figure 1a). To obtain lateral size control of the MQDs, an appropriate modification is made to the hot injection method of our previous study.[26] For the synthesis of WSe_2 MQDs with an average diameter (d) of 5.8 nm, the mixed solution of Ph_2Se_2 (1.0 mmol) and trioctylphosphine oxide (TOPO, 2.0 mmol) is rapidly injected into a three-neck round-bottom flask containing $W(CO)_6$ (0.5 mmol) in TOPO (3.0 mmol) at 330 °C under an Ar atmosphere. Here, the appropriate selection of the ligand with a strong steric barrier (i.e., TOPO) is key to preparing sub-10 nm WSe_2 MQDs because the ligand with its large steric hindrance can slow the growth rate and produce smaller particles,[27] as in the case of CdSe and InAs quantum dot (QD) synthesis.[28,29] The side-view of low-magnification transmission electron microscope (TEM) and the top-view of high-resolution transmission electron microscope (HRTEM) images of the resulting 5.8 nm WSe_2 MQDs show a periodic atomic arrangement of a hexagonal lattice with interlayer spacing of 2.8 and 1.6 Å, which correspond to the (100) and (110) planes, respectively[30] (Figure 1b,c). The binding energies of W $4f_{5/2}$ (34.4 eV), W $4f_{7/2}$ (32.3 eV), Se $3d_{3/2}$ (55.8 eV), and Se $3d_{5/2}$ (54.9 eV), measured using X-ray photoelectron spectroscopy (XPS), indicate that the WSe_2 MQDs adopt a 2H structure[31,32] (Figure S1). In addition, the diameter of the WSe_2 MQDs is controllable by varying the molar ratio of the surfactant to metal precursor. By gradually varying the molar ratio (C_i) from 100 to 5, WSe_2 MQDs with average diameters (d) of 2.5, 4.1, 5.8, and 9.7 nm are obtained (Figure 1d). The controllability of the lateral size is obtained presumably from the controlled surface coverage of the surfactant (i.e., TOPO) on WSe_2 during the synthesis of WSe_2 MQDs. Increasing the number of TOPO molecules on the surface of WSe_2 decreases the growth rate,

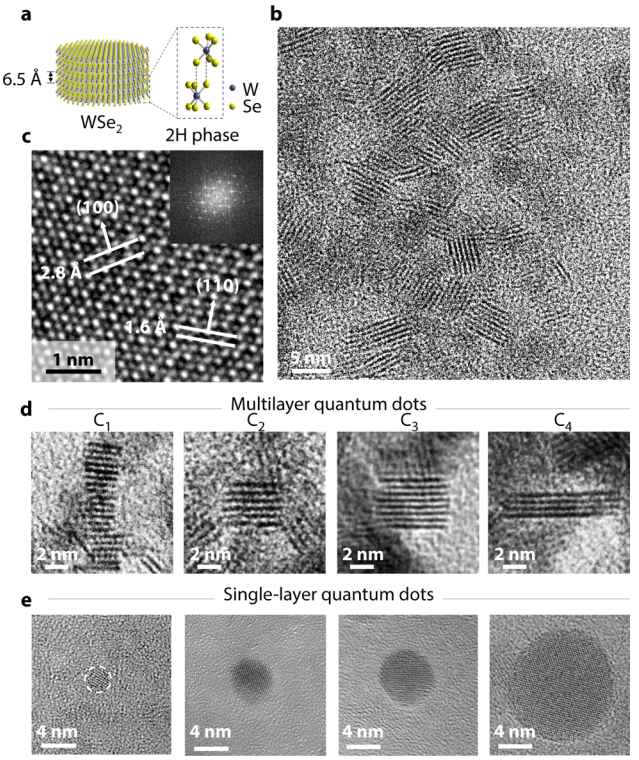

Figure 1. Preparation of single-layer WSe_2 quantum dots (SQDs) with controlled lateral size. (a) Illustration of a colloidal WSe_2 MQD and its 2H trigonal prismatic coordination with the ball-and-stick model. (b) Low-magnification TEM image of 5.8 nm WSe_2 MQDs and (c) high-resolution TEM image of a WSe_2 MQD. Inset shows an FFT pattern of a WSe_2 MQD. (d) TEM images of the side-view of WSe_2 MQDs and (e) top-view of exfoliated WSe_2 SQDs.

therefore producing smaller WSe_2 MQDs.[33] Subsequently, through mild exfoliation of the WSe_2 MQDs, we obtain WSe_2 SQDs that inherit the precontrolled diameter, high crystallinity, and 2H phase of the WSe_2 MQDs (Figure 1e).

To produce WSe_2 SQDs with a controlled diameter from WSe_2 MQDs, the modified TMI method using two different intercalates with different chain lengths is employed (Figure 2a). The TMI method facilitates efficient exfoliation without sonication or reactive chemicals, such as Li^+, and prevents the formation of potential defects in WSe_2 SQDs during the exfoliation process. The low-magnification TEM image shows exfoliated WSe_2 SQDs with d = 4.1 nm (Figure 2b). HRTEM and the fast Fourier transform (FFT) pattern show a highly crystalline hexagonal lattice structure of a WSe_2 SQD without any grain boundary or defects (Figure 2c). The thickness of WSe_2 SQDs exfoliated from MQDs is confirmed by atomic force microscopy (AFM) (Figure 2d). The line profiles of the two selected regions of the AFM image show a height of ∼0.7 nm, which corresponds to the thickness of single-layer WSe_2.[34] The Raman spectra of WSe_2 MQDs show two distinct peaks at 248 and 257 cm^{-1} corresponding to E^1_{2g} (in-plane mode) and A_{1g} (out-of-plane mode), respectively. In WSe_2 SQDs, on the other hand, the merging of the E^1_{2g} and A_{1g} peaks results in a single observable peak at 250 cm^{-1}, consistent with a reported theoretical calculation[35] (Figure 2e). The binding energies of W and Se for d = 4.1 nm WSe_2 SQDs obtained from XPS measurements are also consistent with the previously reported values for 2H WSe_2[31,32] (Figure 2f,g). The above results clearly show that the method reported here produces high-quality

DOI: 10.1021/jacs.6b06972
J. Am. Chem. Soc. 2016, 138, 13253−13259

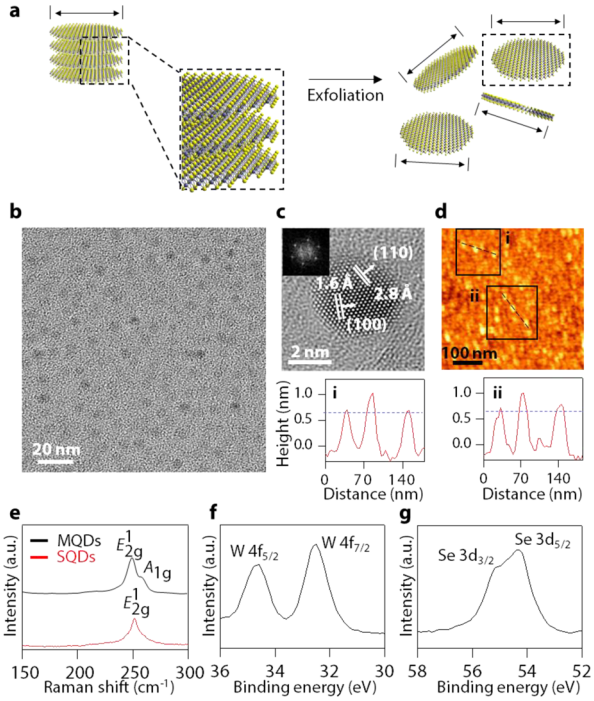

Figure 2. Structural analysis of 4.1 nm colloidal WSe_2 SQDs. (a) Schematic illustration of the exfoliation process from MQDs to SQDs. (b) Low-magnification TEM image of WSe_2 SQDs, and (c) HRTEM image of a WSe_2 SQD. Inset shows its FFT pattern. (d) AFM image of WSe_2 SQDs. The measured height of ~0.7 nm from the line profiles well-matches the theoretical thickness (0.6 nm) of single-layer WSe_2. (e) Raman spectra of WSe_2 MQDs and SQDs. (f,g) XPS spectra of SQDs. The binding energies are as follows; W $4f_{5/2}$ (34.4 eV), W $4f_{7/2}$ (32.3 eV), Se $3d_{3/2}$ (55.8 eV), and Se $3d_{5/2}$ (54.9 eV).

WSe_2 SQDs via TMI of diameter-controlled WSe_2 MQDs. By applying the same procedure to to WSe_2 MQDs of different diameters, we can obtain WSe_2 SQDs with controlled diameters from 2.5 to 9.7 nm (Figure 3a). AFM measurements confirm that the WSe_2 SQDs of all different sizes have a single-layer thickness (Figure S2). The distribution of the diameters of the WSe_2 SQDs with d = 2.5, 4.1, 5.8, and 9.7 nm is shown in Figure 3b, where the standard deviation is on the sub-nm scale.

The PL spectra of the solutions of diameter-controlled WSe_2 SQDs are shown in Figure 3c. The PL spectra of the solution samples of SQDs are obtained at the excitation wavelengths that give the strongest PL intensity for each SQD: 300, 400, 500, and 532 nm for 2.5, 4.1, 5.8, and 9.7 nm WSe_2 SQDs, respectively. The PL quantum yield is 2−3% (e.g., 2.5% for 2.5 nm sample), which is on the similar order of typical magnitude to that of the mechanically exfoliated WS_2 sheets.[36] As the average diameter decreases, the PL peak continuously blue shifts toward 420 nm from that of the large-size (i.e., bulk) single-layer WSe_2 sheets appearing at 750 nm.[34]

The PL from the solutions of WSe_2 SQDs showing a continuous blue shift with decreasing diameter can be similar to the well-known behavior of II−VI QDs, such as CdSe exhibiting confined exciton PL.[37] However, the size-dependent PL from the solutions of WSe_2 SQDs alone is not sufficient to determine its origin. A much broader PL is observed than the exciton PL of single-layer WSe_2 sheets, which suggests possible defect emissions and/or heterogeneous broadening, and the lack of identifiable peaks in the absorption spectra hampers the characterization of the nature of the absorption and emission. We resolve these issues by employing single-particle spectroscopy, providing the clearer spectral features without complications from the ensemble heterogeneity.

We first discuss the single-particle PL and photoluminescence excitation (PLE) spectra from individual WSe_2 SQDs, which are crucial to elucidating the lateral confinement effect on the optical transition energy and the enhanced vibronic coupling that can modify the relaxation pathways of the excited state. The PL and PLE spectra of single WSe_2 SQDs are obtained using a wide-field microscope (Figure 4a) by selecting the area of the CCD image containing one particle and subsequently dispersing the PL with an imaging spectrograph (Figure 4b). The PL spectra are independent of the excitation wavelength (Figure 4c), as expected, from a single WSe_2 SQD, in contrast to the solution PL spectra, which vary with the excitation wavelength due to the remaining size heterogeneity of the ensemble (Figure S4). Figure 4d shows the PL (dot) and PLE (solid) spectra of several single WSe_2 SQDs and the absorption and PL spectra of the A exciton from bulk-size single-layer WSe_2 sheets for comparison.

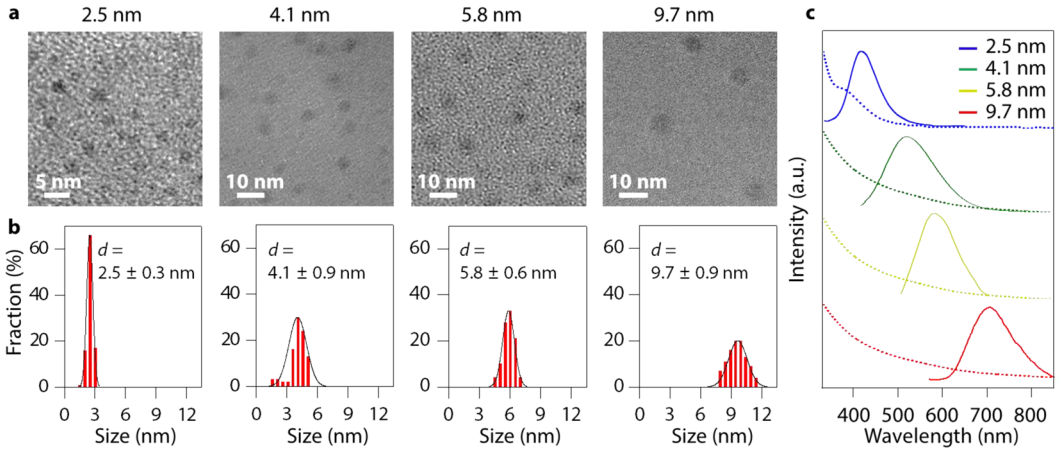

Figure 3. Colloidal WSe_2 SQDs with controlled lateral size and their optical spectra. (a) TEM images of exfoliated WSe_2 SQDs with average diameters (d) ranging from 2.5 to 9.7 nm. (b) Histograms of diameters for WSe_2 SQDs with d = 2.5, 4.1, 5.8, and 9.7 nm, respectively. (c) UV−vis absorption (dot) and PL spectra (solid) of the colloidal solutions of WSe_2 SQDs with d = 2.5, 4.1, 5.8, and 9.7 nm.

DOI: 10.1021/jacs.6b06972
J. Am. Chem. Soc. 2016, 138, 13253−13259

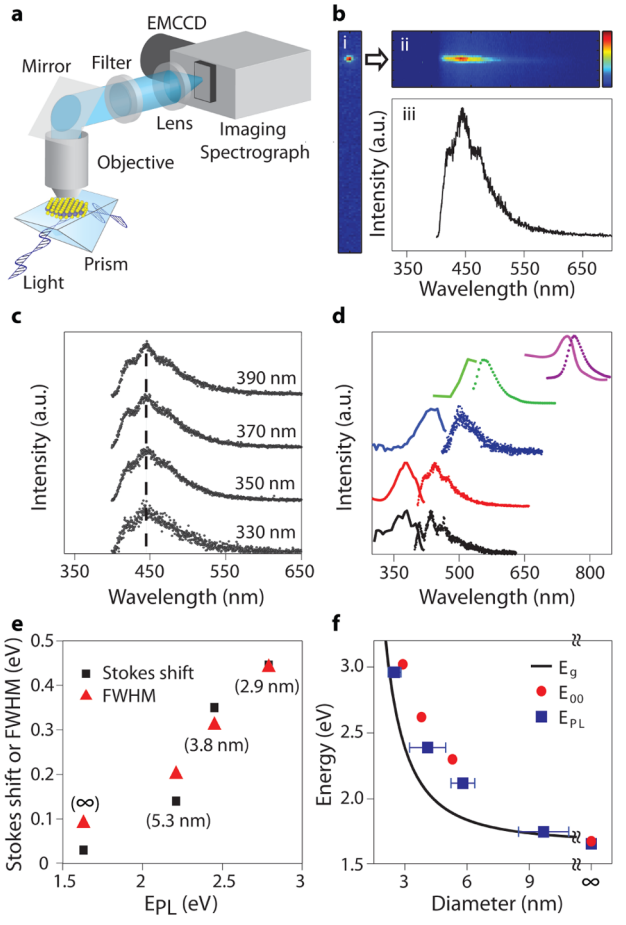

Figure 4. Single-particle PL and PLE measurement of WSe_2 SQDs. (a) Microscope used for the measurement of single WSe_2 SQD PL and PLE. (b) CCD image and PL spectrum from a single WSe_2 SQD. (c) Excitation wavelength-independent PL of a single WSe_2 SQD. (d) PL (dot) and PLE (solid) spectra of several isolated WSe_2 SQDs. The reported PL and absorption from the A exciton of a single-layer WSe_2 sheet at ~750 nm are shown for comparison.[34] (e) PL width (fwhm) and Stokes shift vs peak energy of PL (E_{PL}). The approximate diameter of the WSe_2 SQD, indicated in the parentheses, is estimated from the comparison of E_{PL} with the PL from diameter controlled WSe_2 SQD in solution, whose average diameter is determined from TEM. Under the ∞ sign, the values reported for the single-layer WSe_2 sheets, corresponding to the 2D exciton in single-layer bulk, are shown.[34] (f) Comparison of the 0–0 energy (E_{00}) of single WSe_2 SQDs, E_{PL} of diameter-controlled WSe_2 SQD solution, and band gap (E_g) estimated from the effective mass approximation as a function of diameter (see note S1 in SI).

The PL of single WSe_2 SQDs, while narrower than the solution PL shown in Figure 3c, is still significantly broader than the A exciton PL from single-layer WSe_2 sheets. The PL width (full width at half-maximum, fwhm) increases as the peak energy of the PL increases (E_{PL}), i.e., as the diameter of WSe_2 SQDs decreases, continuously from ~0.1 eV in single-layer WSe_2 sheets to >0.4 eV in WSe_2 SQDs (Figure 4e and Table S1). It is also notable that the PL from the smallest WSe_2 SQD in Figure 4d (black dot) exhibits a distinct multipeak structure reminiscent of the vibronic structure, which gradually disappears as the size of WSe_2 SQDs increases. The same structure is also observed in the PLE spectra, which suggests the presence of a strongly enhanced vibronic coupling in both the absorption and emission of WSe_2 SQDs with decreasing size.

The frequency of the dominant vibrational mode in the vibronic structure, estimated from the gaps between the peaks, has a much higher frequency (~1300 cm^{-1}) than the optical phonon of WSe_2 (~250 cm^{-1}).[35] Considering its high frequency and more prominent presence in the smaller WSe_2 SQDs, the vibronic coupling may involve the bonds between the edge atoms and other molecules bound to them, such as the ligands. In fact, vibronic coupling between the exciton and surface-ligand bonding has also been seen in the PL of II–VI colloidal QDs.[38] These observations indicate that the reduction of the lateral size in WSe_2 SQDs, in addition to increasing the energy of the PL, strongly enhances the vibronic coupling with the edge bonds. One may be inclined to view the broad PL from the strong vibronic coupling as the signature of the defect emission rather than of the radiative recombination of the initially excited state, as often observed in II–VI colloidal QDs with defects. However, this is not the case for WSe_2 SQDs, despite the high edge/area ratio that is potentially capable of producing a high density of trap states; this will become clearer in the following discussions.

The PLE spectra from single WSe_2 SQDs are particularly informative because they exhibit more distinct peaks, in contrast to the solution absorption spectra shown in Figure 3c, and are crucial for examining the lateral confinement effect on the optical transition energy. The more distinct peaks in the single-particle PLE may be the result of the combination of the removal of the size heterogeneity and suppressed radiative relaxation at higher excitation energy, as has been observed in single-layer sheets of several TMCs.[39,40] The line shape of PLE from single WSe_2 SQDs including the vibronic structure is symmetric to that of PL, suggesting that the absorption and PL of WSe_2 SQDs share the same electronic states for the transition. This is further confirmed from the single-particle polarization anisotropy, as discussed later. From the peak energies of the PL and PLE, the effective absorption peak and Stokes shift are estimated. The Stokes shift increases continuously from ~0.03 eV for the A exciton in single-layer WSe_2 sheets to >0.4 eV for WSe_2 SQDs as the diameter of WSe_2 SQDs decreases, further corroborating the strong enhancement effect that the reduction of the lateral size has on the vibronic coupling.

The PLE spectra of single WSe_2 SQDs obtained in the spectral range of this study exhibit one prominent absorption peak, while single-layer WSe_2 sheets are known to exhibit additional higher energy exciton peaks. However, the continuous and smooth evolution of the absorption and PL peak energies of the A exciton in single-layer sheets compared to those of WSe_2 SQDs with decreasing size suggests that the optical transition observed in WSe_2 SQDs has its origin in the A exciton. To examine the effect of the lateral confinement on the optical transition energy in WSe_2 SQDs, the 0–0 energy (E_{00}) obtained from the peak energies of PLE and PL is compared with the size-dependent optical bandgap (E_g) estimated using the effective mass approximation (Figure 4f and note S1 in SI). E_{00} is used instead of the peak energy of PLE or PL in this comparison because of the large and strongly size-dependent Stokes shift. The E_{PL} of the ensemble PL spectra obtained from the diameter-controlled WSe_2 SQD solutions, shown in Figure 3c, is also compared with E_g. While both E_{00} and E_{PL} are higher than the E_g calculated from a simple model that does not account for the potentially size-dependent electron and hole

DOI: 10.1021/jacs.6b06972
J. Am. Chem. Soc. 2016, 138, 13253–13259

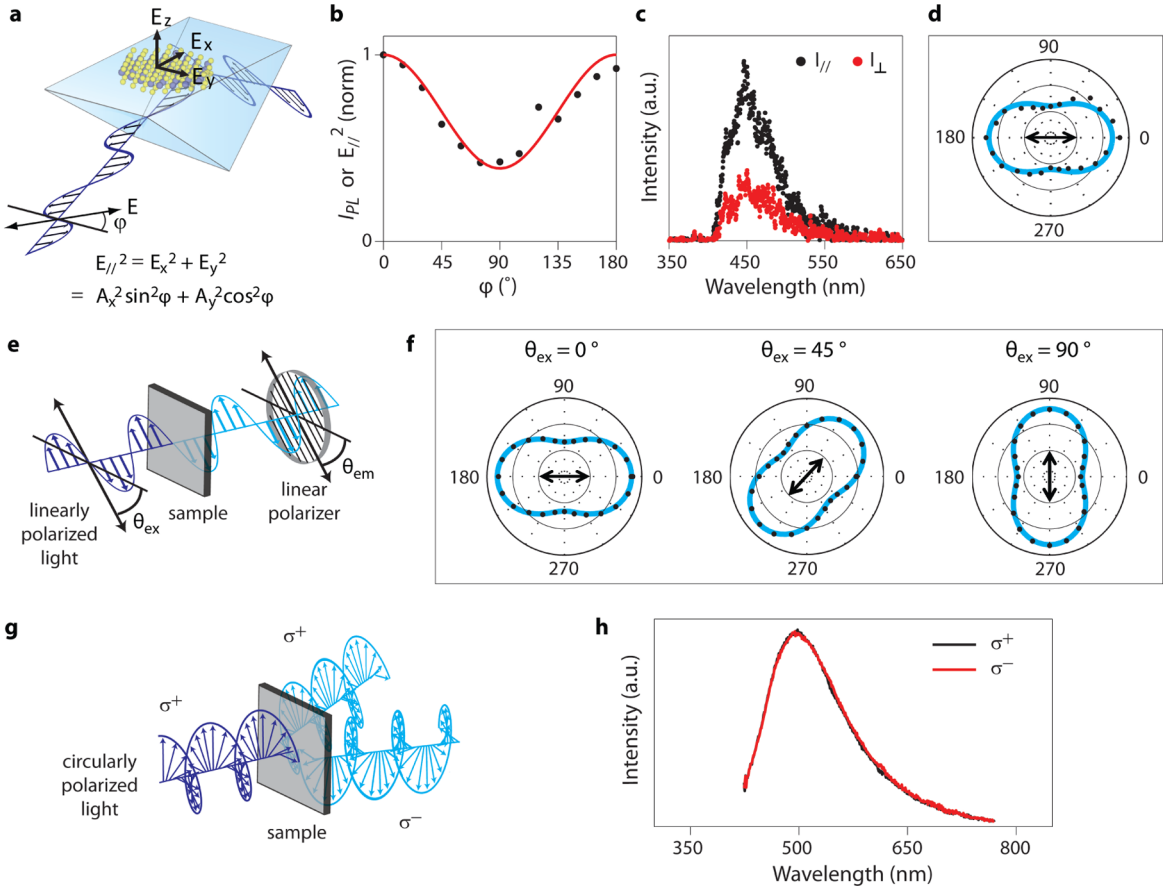

Figure 5. Orientation of the absorption transition dipole and polarization anisotropy measurement. (a) Evanescent field excitation of a WSe_2 SQD under the attenuated total reflection (ATR) scheme. The relative magnitude of the evanescent field parallel ($E_{\parallel}$) and perpendicular ($E_{\perp}$) to the prism surface is controlled by varying the polarization angle (φ) of the incident light. For the parallel component, $E_{\parallel}^2 = E_x^2 + E_y^2 = A_x^2 \sin^2\varphi + A_y^2 \cos^2\varphi$, where A_x and A_y are constants that depend on the angle of incidence and refractive index of the prism. (b) Normalized PL intensity (dot) from a single WSe_2 SQD (I_{PL}) and normalized $E_{\parallel}^2$ (solid) as a function of φ. (c) PL spectra of a single WSe_2 SQD polarized parallel (black) and perpendicular (red) to the excitation polarization. (d) Polar plot of the integrated PL intensity from a single WSe_2 SQD vs emission polarization angle for the excitation polarization angle of 0°. Arrows indicate the excitation polarization direction. The data in panels (b–d) are obtained from the same single WSe_2 SQD excited at 370 nm. (e) PL polarization anisotropy measurement on a WSe_2 SQD film under linearly polarized far-field excitation. θ_{ex} and θ_{em} are the excitation and emission polarization angles, respectively. (f) Polar plot of the integrated PL intensity vs θ_{em} from the WSe_2 SQD film at θ_{ex} = 0°, 45°, and 90° and an excitation wavelength of 405 nm. (g) Circular PL polarization anisotropy measurement on the WSe_2 SQD film (see Figure S6). (h) PL spectra from the WSe_2 SQD film with right-handed (σ^+, black) or left-handed (σ^-, red) circular polarization for σ^+ excitation at 405 nm.

effective masses and dielectric constant in colloidal WSe_2 SQDs, both have a similar range of diameters exhibiting a strong size dependence.

The single-particle PLE and PL spectra of WSe_2 SQDs discussed above provide valuable insights into the evolution of the optical transition energy and vibronic coupling in WSe_2 SQDs from their 2D counterpart, i.e., the A exciton in single-layer WSe_2 sheets, as the lateral confinement is imposed. Further examination of the similarities and differences between WSe_2 SQDs and single-layer WSe_2 sheets is performed via single-particle PL polarization anisotropy measurements. In single-layer WSe_2 sheets, the transition dipole of the A exciton is in-plane and 2D isotropic, and the polarization of the PL correlates well with the excitation polarization for linearly polarized excitation.[41,42] For circularly polarized excitation, valley polarization results in a circularly polarized PL from the A exciton.[41] Here, we examine whether such properties of 2D excitons are preserved in colloidal WSe_2 SQDs with strong lateral confinement. Because the shape of WSe_2 SQDs is highly symmetric, the transition dipole of the absorption that gives rise to the PL in WSe_2 SQDs is also expected to be in-plane and 2D isotropic. This is confirmed by measuring the PL intensity from a single WSe_2 SQD under an evanescent field excitation (Figure 5a and note S2 in SI), where the magnitude of the evanescent field parallel ($E_{\parallel}$) and perpendicular ($E_{\perp}$) to the substrate can be varied by changing the input polarization angle (φ). Because WSe_2 SQDs lie parallel to the surface of the prism, the PL intensity (I_{PL}) should be linear only with $E_{\parallel}^2$ if the transition dipole is in-plane and 2D isotropic. Figure 5b, showing the identical variation of I_{PL} (dot) and $E_{\parallel}^2$ (solid) with φ, indicates that the orientation of the absorption dipole in WSe_2 SQDs is the same as that in single-layer WSe_2 sheets.

Having established the orientation of the absorption transition dipole, we measure the linear polarization anisotropy of the PL from a single WSe_2 SQD. If the defect emission dominates the PL from WSe_2 SQDs, as presumed in some earlier studies,[43] the polarization anisotropy should be lost similarly to the defect emission from colloidal II–VI QDs.[44] Figure 5c compares the PL spectra of a single WSe_2 SQD polarized parallel ($I_{\parallel}$) and perpendicular ($I_{\perp}$) to the direction of

DOI: 10.1021/jacs.6b06972
J. Am. Chem. Soc. 2016, 138, 13253–13259

excitation polarization, which indicates a clear presence of polarization anisotropy. Figure 5d shows the polar plots of the integrated PL intensity vs emission polarization angle (θ_{em}) for the excitation polarization angle of $\theta_{ex} = 0°$. Interestingly, the linear polarization anisotropy, defined as $r = (I_{\parallel} - I_{\perp})/(I_{\parallel} + 2I_{\perp})$, from the WSe_2 SQD is nearly the same as that for the A exciton PL ($r = \sim 0.25$) in single-layer WSe_2 sheets reported earlier.[42] This is surprising considering that WSe_2 SQDs with a large edge/area ratio can potentially create a high density of trap states at the edges compared to large-size sheets prepared via exfoliation of the bulk or chemical vapor deposition. The absence of the signature of defects in the PL also supports the high quality of the colloidal WSe_2 SQDs synthesized here. Another interesting property expected from the colloidal WSe_2 SQDs possessing a 2D isotropic transition dipole is that the ensemble of SQDs deposited on a substrate with random in-plane orientation can still exhibit the optical properties of a perfectly oriented assembly. This behavior, in contrast to QDs made from 3D crystals such as CdSe QDs, is verified by measuring the PL polarization anisotropy of a WSe_2 SQD film deposited on a substrate under linearly polarized far-field excitation using the setup shown in Figure 5e. Figure 5f shows the polar plots of the integrated PL intensity from the WSe_2 SQD film vs emission polarization angle (θ_{em}) for three different excitation polarization angles of $\theta_{ex} = 0°$, 45°, and 90°, which exhibit a polarization anisotropy nearly identical to that of the single WSe_2 SQD. On the other hand, the circular PL polarization anisotropy, resulting from the valley polarization present in single-layer WSe_2 sheets, is not observed in WSe_2 SQDs. For the circularly polarized excitation (Figures 5g and S6), the WSe_2 SQD film shows identical PL spectra and intensities for the two opposite helicities at ~10 K (Figure 5h). The loss of circular polarization anisotropy in WSe_2 SQDs may be caused by the possible enhancement of the intervalley scattering from the strong lateral confinement and close proximity of the edges.[45]

CONCLUSION

In conclusion, we developed a facile and effective process for producing high-quality size-controlled WSe_2 SQDs which consists of the colloidal synthesis of WSe_2 MQDs with lateral size controllability and subsequent exfoliation of MQDs. This methodology allows us to explore the lateral confinement effects on the unique optical properties originating from 2D excitons in single-layer TMCs. The single-particle PLE and PL spectra of WSe_2 SQDs clearly reveal not only the lateral confinement effect on the optical transition energy but also the enhanced vibronic coupling due to the proximity of the edge bonds resulting in a large increase in the Stokes shift and spectral width. Furthermore, single-particle polarization spectroscopy shows that the absorption and emission of colloidal WSe_2 SQDs exhibit the same in-plane, 2D isotropic transition dipole and linear PL polarization anisotropy as those of the 2D exciton in the single-layer sheets of WSe_2. On the other hand, the circular polarization anisotropy observed in single-layer TMC sheets is absent in WSe_2 SQDs, indicating that the valley polarization is lost in the laterally confined single-layer TMCs.

EXPERIMENTAL SECTION

Size-Controlled Synthesis of WSe_2 MQDs. *2.5 nm MQDs.* Tungsten hexacarbonyl ($W(CO)_6$, 0.5 mmol) is first added to trioctylphosphine oxide (TOPO, 48 mmol) in a three-neck round-bottom flask and heated to 330 °C at a rate of 5 °C/min under Ar flow. Then, a mixture of diphenyl diselenide (Ph_2Se_2, 1.0 mmol) dissolved in TOPO (2.0 mmol) is rapidly injected. After 1 h, the solution is cooled to room temperature and washed with a mixture of hexane and methanol (2:1 by volume) several times.

4.1, 5.8 and 9.7 nm MQDs. When the molar ratio of TOPO to $W(CO)_6$ is reduced to 50, 10, and 5, WSe_2 MQDs with diameters of 4.1, 5.8, and 9.7 nm, respectively, are obtained.

Exfoliation of WSe_2 MQDs to SQDs. WSe_2 MQDs (10 mg, 0.03 mmol), sodium ethoxide (0.136 g, 2 mmol), and sodium hexanolate (0.1 g, 1 mmol) are mixed in DMSO (10 mL) and stirred for 8 h at room temperature. After the removal of nonexfoliated WSe_2 by centrifugation at 3,000 rpm for 2 min, the supernatant is then centrifuged at 15,000 rpm for 1 h. The isolated SQDs are washed with a mixture of deionized water (DIW), ethanol, and hexane (1:1:1 by volume) several times and dispersed in DIW for further characterization. The exfoliation yield is 33%.

Instruments. TEM and HRTEM are measured by using a JEM 2100 at 200 kV and a JEOL-ARMI 1300S at 1250 kV. AFM images are obtained using the noncontact mode of a scanning probe microscope (Veeco). Raman spectra are obtained with a LabRam Aramis (Horiba) using the 532 nm line for excitation at a power of 0.5 W. XPS data are obtained with a K-alpha (Thermo Fisher Scientific) using a 1486.6 eV X-ray delivered by an Al μ-focusing monochromator.

Measurement of Single-Particle PL and PLE Spectra. The single-particle PL spectra from individual single-layer WSe_2 quantum dots (SQDs) are measured with a home-built wide-field microscope equipped with an imaging spectrograph (Princeton Instruments, Acton SpectraPro SP-2300) and an electron multiplying charge-coupled device (EMCCD) (Princeton Instruments, ProEM 16002). A Xe-lamp (Oriel Instrument, 300 W) in conjunction with a monochromator (Newport, Oriel Cornerstone 130) provides the tunable excitation light in the UV−vis region. Excitation of WSe_2 SQDs is performed via an ATR scheme using a quartz prism to minimize the interference from the excitation light during the PL measurement. A highly diluted colloidal suspension of WSe_2 SQDs is drop casted onto a thin quartz plate to deposit well-separated WSe_2 SQDs, and the plate is placed on top of the prism using an index matching liquid. The PL from a single WSe_2 SQD collected with an objective (Olympus, PLanFL N 40×) is focused on the EMCCD either as an image or as a spectrum using a tube lens (Nikon) through the imaging spectrograph. The PLE spectra are obtained by measuring the integrated PL intensity as a function of the excitation wavelength with a 10 nm bandwidth after a spectral calibration of the entire optical system with CdSe quantum dots, which have a well-known PLE profile.

Measurement of the Absorption Transition Dipole Orientation and Polarization Anisotropy. The orientation of the absorption transition dipole of a single WSe_2 SQD is determined using the same setup used for the single-particle PL and PLE measurements. The magnitude of the parallel ($E_{\parallel}$) and perpendicular ($E_{\perp}$) components of the evanescent field at the surface of the prism, with exciting WSe_2 SQDs lying flat on the surface, is controlled by varying the polarization angle (φ) of the excitation light entering the prism. The wavelength of excitation (370 nm, 10 nm bandwidth from the Xe-lamp) is set at the peak of the PLE for the chosen WSe_2 SQD. The PL intensity of the single WSe_2 SQD is measured as a function of φ, which is later compared with $E_{\parallel}^2$ (φ). For the measurement of the linear polarization anisotropy of the single WSe_2 SQD, the evanescent field polarized along the y-axis ($\theta_{ex} = 0°$) is used for the excitation. The PL spectra and intensities are measured as a function of the angle of the analyzer placed between the objective and EMCCD. The circular polarization anisotropy is measured using the ensemble of WSe_2 SQDs deposited on a sapphire window using an optical cryostat (Janis ST-100) at 10 K. The PL spectra with two opposite helicities (σ^+ and σ^-) are recorded under circularly polarized excitation light (σ^+) at 405 nm. Further details on the circular polarization anisotropy measurement are included in Figure S6.

DOI: 10.1021/jacs.6b06972
J. Am. Chem. Soc. 2016, 138, 13253−13259

■ ASSOCIATED CONTENT

Supporting Information

The Supporting Information is available free of charge on the ACS Publications website at DOI: 10.1021/jacs.6b06972.

Detailed analysis and methods (PDF)

■ AUTHOR INFORMATION

Corresponding Authors

*dhson@chem.tamu.edu

*jcheon@yonsei.ac.kr

Author Contributions

⊥These authors contributed equally.

Notes

The authors declare no competing financial interest.

■ ACKNOWLEDGMENTS

This work was supported by the Institute for Basic Science (IBS-R026-D1), the Asian Office of Aerospace Research and Development (FA2386-14-1-0014), the Welch Foundation (grant no. A-1639), NSF (grant no. DMR-1404457), and S. J. Yoo for TEM analyses [KBSI-HVEM (JEM-ARM1300S)].

■ REFERENCES

(1) Wang, Q. H.; Kalantar-Zadeh, K.; Kis, A.; Coleman, J. N.; Strano, M. S. *Nat. Nanotechnol.* **2012**, *7*, 699−712.

(2) Chhowalla, M.; Shin, H. S.; Eda, G.; Li, L. J.; Loh, K. P.L; Zhang, H. *Nat. Chem.* **2013**, *5*, 263−275.

(3) Tan, C.; Zhang, H. *Nat. Commun.* **2015**, *6*, 7873.

(4) Zhang, H. *ACS Nano* **2015**, *9*, 9451−9469.

(5) Tan, C.; Zhang, H. *Chem. Soc. Rev.* **2015**, *44*, 2713−2731.

(6) Chen, J.; Wu, X.; Yin, L.; Li, B.; Hong, X.; Fan, Z.; Chen, B.; Xue, C.; Zhang, H. *Angew. Chem., Int. Ed.* **2015**, *54*, 1210−1214.

(7) Zhao, W. J.; Ghorannevis, Z.; Chu, L.; Toh, M.; Kloc, C.; Tan, P. H.; Eda, G. *ACS Nano* **2013**, *7*, 791−797.

(8) Mak, K. F.; Lee, C.; Hone, J.; Shan, J.; Heinz, T. F. *Phys. Rev. Lett.* **2010**, *105*, 136805.

(9) Splendiani, A.; Sun, L.; Zhang, Y.; Li, T.; Kim, T.; Kim, J.; Chim, C. Y.; Galli, G.; Wang, F. *Nano Lett.* **2010**, *10*, 1271−1275.

(10) Eda, G.; Yamaguchi, H.; Voiry, D.; Fujita, T.; Chen, M.; Chhowalla, M. *Nano Lett.* **2011**, *11*, 5111−5116.

(11) Gutiérrez, H. R.; López, N. P.; Elías, A. L.; Berkdemir, A.; Wang, B.; Lv, R.; Urías, F. L.; Crespi, V. H.; Terrones, H.; Terrones, M. *Nano Lett.* **2013**, *13*, 3447−3454.

(12) Li, H.; Wu, J.; Yin, Z.; Zhang, H. *Acc. Chem. Res.* **2014**, *47*, 1067−1075.

(13) Xiao, D.; Liu, G. B.; Feng, W. X.; Xu, X. D.; Yao, W. *Phys. Rev. Lett.* **2012**, *108*, 196802.

(14) Cao, T.; Wang, G.; Han, W.; Ye, H.; Zhu, C.; Shi, J.; Niu, Q.; Tan, P.; Wang, E.; Liu, B.; Feng, J. *Nat. Commun.* **2012**, *3*, 887.

(15) Mak, K. F.; He, K. L.; Shan, J.; Heinz, T. F. *Nat. Nanotechnol.* **2012**, *7*, 494−498.

(16) Ross, J. S.; Wu, S.; Yu, H.; Ghimire, N. J.; Jones, A. M.; Aivazian, G.; Yan, J.; Mandrus, D. G.; Xiao, D.; Yao, W.; Xu, X. *Nat. Commun.* **2013**, *4*, 1474.

(17) Mak, K. F.; He, K.; Lee, C.; Lee, G. H.; Hone, J.; Heinz, T. F.; Shan, J. *Nat. Mater.* **2013**, *12*, 207−211.

(18) Wang, G.; Bouet, L.; Lagarde, M. V.; Balocchi, A.; Amand, T.; Marie, X.; Urbaszek, B. *Phys. Rev. B: Condens. Matter Mater. Phys.* **2014**, *90*, 075413.

(19) Dai, W. H.; Dong, H.; Fugetsu, B.; Cao, Y.; Lu, H.; Ma, X.; Zhang, X. *Small* **2015**, *11*, 4158−4164.

(20) Gopalakrishnan, D.; Damien, D.; Shaijumon, M. M. *ACS Nano* **2014**, *8*, 5297−5303.

(21) Lin, L. X.; Xu, Y.; Zhang, S.; Ross, I. M.; Ong, A. C.; Allwood, D. A. *ACS Nano* **2013**, *7*, 8214−8223.

(22) Zhang, X.; Lai, Z.; Liu, Z.; Tan, C.; Huang, Y.; Li, B.; Zhao, M.; Xie, L.; Huang, W.; Zhang, H. *Angew. Chem., Int. Ed.* **2015**, *54*, 5425−5428.

(23) Ha, H. D.; Han, D. J.; Choi, J. S.; Park, M.; Seo, T. S. *Small* **2014**, *10*, 3858−3862.

(24) Xu, S. J.; Li, D.; Wu, P. Y. *Adv. Funct. Mater.* **2015**, *25*, 1127−1136.

(25) Jeong, S.; Yoo, D.; Ahn, M.; Miró, P.; Heine, T.; Cheon, J. *Nat. Commun.* **2015**, *6*, 5763.

(26) Jung, W.; Lee, S.; Yoo, D.; Jeong, S.; Miró, P.; Kuc, A.; Heine, T.; Cheon, J. *J. Am. Chem. Soc.* **2015**, *137*, 7266−7269.

(27) Krommenhoek, P. J.; Wang, J.; Hentz, N.; Johnston-Peck, A. C.; Kozek, K. A.; Kalyuzhny, G.; Tracy, J. B. *ACS Nano* **2012**, *6*, 4903−4911.

(28) Murray, C. B.; Norris, D. J.; Bawendi, M. G. *J. Am. Chem. Soc.* **1993**, *115*, 8706−8715.

(29) Green, M.; Norager, S.; Moriarty, P.; Motevalli, M.; O'Brien, P. *J. Mater. Chem.* **2000**, *10*, 1939−1943.

(30) JCPDS, *International Centre for Diffraction Data*, 1997. PDF-2 File No. 38-1388 (WSe_2). http://www.icdd.com/products/pdf2.htm, accessed March 10, 2015.

(31) Guo, J. H.; Shi, Y. T.; Bai, X. G.; Wang, X. C.; Ma, T. L. *J. Mater. Chem. A* **2015**, *3*, 24397−24404.

(32) Liu, Z.; Zhao, H.; Zhang, Y.; Zhang, X.; Du, Y. *Inorg. Chem. Front.* **2016**, *3*, 313−319.

(33) Pradhan, N.; Reifsnyder, D.; Xie, R. G.; Aldana, J.; Peng, X. G. *J. Am. Chem. Soc.* **2007**, *129*, 9500−9509.

(34) Huang, J. K.; Pu, J.; Hsu, C. L.; Chiu, M. H.; Juang, Z. Y.; Chang, Y. H.; Chang, W. H.; Iwasa, Y.; Takenobu, T.; Li, L. J. *ACS Nano* **2014**, *8*, 923−930.

(35) Luo, X.; Zhao, Y.; Zhang, J. L.; Toh, M.; Kloc, C.; Xiong, Q.; Quek, S. Y. *Phys. Rev. B: Condens. Matter Mater. Phys.* **2013**, *88*, 195313.

(36) Yuan, L.; Huang, L. *Nanoscale* **2015**, *7*, 7402−7408.

(37) Norris, D. J.; Bawendi, M. G. *Phys. Rev. B: Condens. Matter Mater. Phys.* **1996**, *53*, 16338−16346.

(38) Lifshitz, E. *J. Phys. Chem. Lett.* **2015**, *6*, 4336−4347.

(39) Kozawa, D.; Kumar, R.; Carvalho, A.; Amara, K. K.; Zhao, W.; Wang, S.; Toh, M.; Ribeiro, R. M.; Castro Neto, A. H.; Matsuda, K.; Eda, G. *Nat. Commun.* **2014**, *5*, 4543.

(40) Hill, H. M.; Rigosi, A. F.; Roquelet, C.; Chernikov, A.; Berkelbach, T. C.; Reichman, D. R.; Hybertsen, M. S.; Brus, L. E.; Heinz, T. F. *Nano Lett.* **2015**, *15*, 2992−2997.

(41) Schuller, J. A.; Karaveli, S.; Schiros, T.; He, K.; Yang, S.; Kymissis, L.; Shan, J.; Zia, R. *Nat. Nanotechnol.* **2013**, *8*, 271−276.

(42) Jones, A. M.; Yu, H.; Ghimire, N. J.; Wu, S.; Aivazian, G.; Ross, J. S.; Zhao, B.; Yan, J.; Mandrus, D. G.; Xiao, D.; Yao, W.; Xu, X. *Nat. Nanotechnol.* **2013**, *8*, 634−638.

(43) Gopalakrishnan, D.; Damien, D. L.; Li, B.; Gullappalli, H.; Pillai, V. K.; Ajayan, P. M.; Shaijumon, M. M. *Chem. Commun.* **2015**, *51*, 6293−6296.

(44) Montiel, D.; Yang, H. *J. Phys. Chem. A* **2008**, *112*, 9352−9355.

(45) Saraiva, A. L.; Calderon, M. J.; Hu, X. D.; Das Sarma, S.; Koiller, B. *Phys. Rev. B: Condens. Matter Mater. Phys.* **2009**, *80*, 081305.